

Reconstruction of Complex Shape Buildings from Lidar Data Using Free Form Surfaces

Nizar Abo Akel, Sagi Filin, and Yerach Doytsher

Abstract

Building reconstruction from lidar data offers promising prospects for rapid generation of large-scale 3D models autonomously. Such reconstruction requires knowledge on a variety of parameters that refer to both the point cloud and the modeled buildings. The complexity of the reconstruction task has led researchers to use external information to localize buildings and assume that they consist of only planar parts. These assumptions limit the reconstruction of complex buildings, particularly those having curved faces. We present in this paper a detection and reconstruction model that considers the point cloud as the only information source and supports the reconstruction of general shape surfaces. Nonetheless, since many of the buildings are composed of planar faces, we maintain the planar based partitioning whenever possible and model non-planar surfaces only where needed. This way, standard models are extended to support free-form roof shapes without imposing artificial models. In addition to the free-form surface extension, we demonstrate the effect of imposing geometric constraints on the reconstruction as a means to generate realistic building models.

Introduction

Three-dimensional reconstruction of buildings becomes a fundamental part in a growing number of applications, such as urban planning, telecommunications, and environmental monitoring, as only a few examples. The extent of urban regions and the labor involved in a manual reconstruction of their shape has motivated research into semi- and fully-automatic reconstruction techniques from remotely sensed data. Among the candidate data sources, airborne laser scanning emerged in recent years as a leading information source for extraction and reconstruction of buildings. This realization is reflected by a growing number of publications that report using lidar data as their primary data source, noting the direct acquisition of accurate and dense 3D data as key contributors towards autonomous reconstruction (e.g., Brenner and Haala, 1998; Vosselman, 1999; Wang and Schenk, 2000; Brenner, 2000; Voegtle *et al.* 2005; Rottensteiner *et al.*, 2005).

Extraction of buildings from lidar data is usually divided into two parts where the first involves their detection within the point cloud, and the second reconstruction of their 3D shape. For their detection, Wang (1998) proposes edge operators to localize buildings in a point cloud. Oda *et al.* (2004) isolate building patches by applying morphological opening filters to identify the terrain and then subtract it from the digital surface model (DSM). Alharthy and Bethel

(2004) propose a local segmentation to identify detached solid objects. Seo and Schenk (2003) use contour graphs to compute slopes between contours and through them extract building boundaries. Others like Vosselman and Dijkman (2001) and Schwalbe *et al.* (2004) make use of external data in the form of ground plans to localize buildings.

Shape reconstruction involves selecting a descriptive geometrical representation and an extraction strategy for the roof primitives. For the geometric representation, three main categories can be noted including, the boundary representation (B-REP), the parametric representation, and the Constructive Solid Geometry (CSG) model. The B-REP (see Mäntylä, 1988) is essentially a polyhedral model where the object surfaces are described by their boundary lines and surfaces. This model enables the representation of generic building types but does not have an inherent support for geometric constraints among the entities composing it. The parametric representation describes buildings as a set of parameters, e.g., length, width, height, and others, but the reconstructed building shapes are limited to certain types of predefined models (see Maas and Vosselman, 1999; Brenner and Halla, 1998). The CSG model represents buildings as composed of a set of parts that are modeled in a tree structure; nodes in the tree hold the building parts, and edges, the operations among them (e.g., union, intersection, difference). These operations allow grouping building parts into complete models (Vosselman and Dijkman, 2001). As for the extraction of the roof primitives, in almost all cases, the segmentation of the point cloud will seek partition into a set of planar faces. Voegtle *et al.* (2005) use classified data as an input, where the extraction of the roof planes is region growing based with a homogeneity predicate. Rottensteiner *et al.* (2005) describe a roof delineation algorithm where the classified data is segmented in a similar fashion as in Voegtle *et al.* (2005). The boundaries of the detected planes are determined using the Voronoi diagram, and the resulting edges are then grouped together into polyhedral models. In Rottensteiner (2006), the estimation of the building parameters using an adjustment model of all observations is added. Haala *et al.* (2006) describe an approach for 3D building reconstruction that is based on cell decomposition. The authors use 2D ground plans and 3D point clouds both from airborne and terrestrial scanners. Similar to Vosselman and Dijkman (2001) and Schwalbe *et al.* (2004), ground plans are used to create a set of space dividing planes (termed cells by the

Photogrammetric Engineering & Remote Sensing
Vol. 75, No. 3, March 2009, pp. 271–280.

0099-1112/09/7503-0271/\$3.00/0

© 2009 American Society for Photogrammetry
and Remote Sensing

Department of Transportation and Geo-Information Engineering,
Technion City, Haifa 32000, Israel (filin@tx.technion.ac.il).

authors). Each cell is extruded and the points inside of it are used to construct the roof.

While a large body of research has been devoted into building reconstruction, many challenges remain unanswered. One such challenge concerns the general planar roof-face assumption that is common to almost all reconstruction models. While planar roof-face buildings are still the majority, buildings with general roof shape can be found in almost every scene. Applying planar-based models will lead to an artificial roof partitioning and a flawed reconstruction. Therefore, improving the reliability of the process, the reconstruction process should support modeling of general roof shapes. Nonetheless, as many of the buildings are still composed of planar faces, a planar based partitioning is an appealing concept to maintain whenever possible. An optimal reconstruction model will therefore support the representation for curved surfaces, but will be able deciding when planarity fails to hold and a more elaborate description is needed.

We present in this paper a model that supports the reconstruction of general building shapes. The algorithm assumes no prior information about their location or shape, and considers the raw point cloud as the only data source. Differing from most of the prevailing reconstruction models, it supports modeling planar and non-planar roofs. In the following section, we outline the proposed detection and reconstruction model. Next, we describe the reconstruction model for non-planar roof faces. Results of the proposed model and discussion on its properties conclude the presentation.

Building Detection and Reconstruction

The proposed reconstruction framework is composed of the following steps: (a) detection of buildings in the point cloud, (b) segmentation of the roof into faces and analysis of the segmentation results, and (c) geometric adjustment for the building primitives. Within this framework, the reconstruction of non-planar roof faces falls within the second phase (see Process Flow in Figure 1). We present first, in short, the

reconstruction model as a whole, and then elaborate on the modeling of general shaped surfaces, which is thereby placed in context.

Building Detection

The proposed building detection strategy is based on filtering detached objects in the point cloud from the terrain. Since buildings are distinct objects compared to their surrounding, most filtering algorithms should perform well in their separation (Sithole and Vosselman, 2004). The applied filtering model follows Abo Akel *et al.* (2007) and makes use of global orthogonal polynomials functions as a coarse terrain representation for separating the detached objects from the terrain. The model then applies a surface refinement procedure for adding the fine terrain details that were ignored by the coarse modeling but conform to the general terrain shape (Abo Akel *et al.*, 2007). The filtering output is the set of terrain points, but here our interest is in the set of detached segments that include buildings as well as other objects. The detached objects are filtered further by eliminating segments that are either too small (namely area too small to form a building; we set it to 50 m²) or too close to the bare earth (this we define as 2.5 m). These two simple filters remove a significant amount of spurious segments and save the need to filter them in the following phase. The remaining ones are being probed further in the subsequent classification and segmentation phase.

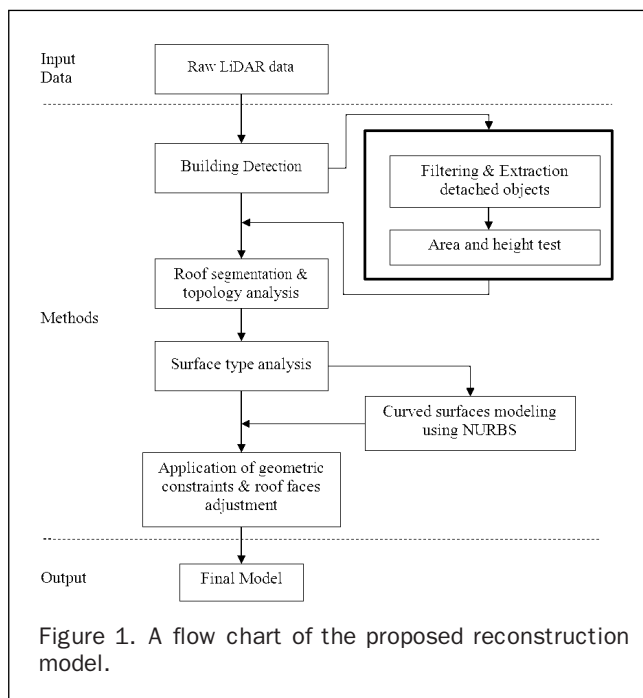
Segmentation

The detached regions are further classified and segmented via cluster analysis that uses local surface parameters as attributes (we use the model proposed in Filin and Pfeifer (2006)). With these attributes, solid roof surfaces tend to cluster as they share slope parameters while vegetation or vegetation-like segments do not (and therefore filtered out). Clusters that share common surface properties constitute “surface classes” that may consist of more than one physical segment. Therefore, following the extraction of a “surface class,” physical segments in object space are extracted by linking points according to proximity measures. The identified surface segments are validated via surface fitting and then extended, if possible, by adding un-segmented points and by merging segments that share similar surface properties. Segment merging is decided by testing whether neighboring segments share similar mean (the estimated surface parameters) and standard deviation. The size of the segments is controlled by *std.* thresholds. An upper bound limit, σ_{max} , that reflects physical surface accuracy is set to avoid over-segmentation. Additionally, a lower bound, σ_{min} , that reflects the expected accuracy of the laser points, is applied to avoid under-segmentation.

Topology and Geometric Adjustment

The extracted segments define individual roof elements but not the actual geometry. The subsequent phase therefore models geometric and topological relations, allowing transforming the primitives into a building model.

Roof topology and approximated shape are established using the topological relations among the individual parts. For the reconstruction, the relevant relations are adjacency and inclusion (the latter refers to dormers mostly). These relations are established by analyzing the connectivity between the boundary points of the extracted segments. Usually, adjacent segments will form a crease-edge where the two surface patches intersect. These intersections form ridgelines that establish the roof geometry. Adjacency and inclusion can also exist between discontinuous surfaces; mainly ones that are linked by a step-edge. Such discontinuities can be identified by analyzing the slope between the edge-points that link the



neighboring segments and the relative location of the intersecting line. A plane that passes between the segments is then adjusted using the bounding points. Finally, lines defining the outline of the building (and dormers) complete the roof geometry. These cannot be constrained geometrically using plane intersection, and since laser scanners do not capture well linear features, they are not well defined. These bounding lines are approximated using the classical application of the Hough transform for line detection while constraining them to lie on the surface defined by the segment.

Shape Refinement by Means of Geometric Constraints

Manmade objects tend to form relatively simple shapes characterized by simple geometric relations like parallelism and orthogonality. Generally, the extracted lines (both crease-edges and boundaries) will not follow these relations and will have to be adjusted using a set of 3D constraints. These constraints should correct the building geometry without tempering with the topology. As lines with different levels of accuracy are extracted, the implementation of the adjustment weights in their accuracy and reliability. The extracted lines are classified into two categories: (a) *crease edges* that refer to lines extracted from the intersection of two neighboring segments, and (b) *border lines* that refer to the outline and are less accurate.¹ A distinction is made between relations among lines from the first category and relations between lines from the second category against lines from the first and among themselves. The adjustment is performed using the constraints model:

$$w = Cx \quad (1)$$

which is solved by

$$x = P^{-1}C^T(CP^{-1}C^T)^{-1}w \quad (2)$$

with C , the coefficient matrix for the constraints, x , the coordinate of the unknown points, w , the residual vector for constraints before the adjustment, and P , the weight matrix. Stronger weights are assigned to crease-edge intersections (first category) than to those involving intersections with borderlines, which are of lower accuracy. The constraints are applied to the end-points and are realized as follows:

Parallelism for two lines in 3D space is achieved by correcting the end-points of each edge, which translates into two constraints:

$$\begin{aligned} \frac{(X_A + \Delta X_A) - (X_B + \Delta X_B)}{(Y_A + \Delta Y_A) - (Y_B + \Delta Y_B)} &= \frac{(X_C + \Delta X_C) - (X_D + \Delta X_D)}{(Y_C + \Delta Y_C) - (Y_D + \Delta Y_D)} \\ \frac{(X_A + \Delta X_A) - (X_B + \Delta X_B)}{(Z_A + \Delta Z_A) - (Z_B + \Delta Z_B)} &= \frac{(X_C + \Delta X_C) - (X_D + \Delta X_D)}{(Z_C + \Delta Z_C) - (Z_D + \Delta Z_D)} \end{aligned} \quad (3)$$

with X_i , Y_i , Z_i , the endpoint coordinates, and ΔX_i , ΔY_i , ΔZ_i , the corrections ($i = \{A, B, C, D\}$ refer to edges AB, CD). Following the elimination of second-order terms, the forms in Equation 3 can be written as (with $X_{ij} = X_i - X_j$):

$$\begin{aligned} X_{CD} Y_{AB} - X_{AB} Y_{CD} &= Y_{CD}\Delta X_A + X_{DC}\Delta Y_A + Y_{DC}\Delta X_B + X_{DC}\Delta Y_B \\ &\quad + Y_{BA}\Delta X_C + X_{AB}\Delta Y_C + Y_{AB}\Delta X_D + X_{BA}\Delta Y_D \\ X_{CD} Z_{AB} - X_{AB} Z_{CD} &= Z_{CD}\Delta X_A + X_{DC}\Delta Z_A + Z_{DC}\Delta X_B + X_{DC}\Delta Z_B \\ &\quad + Z_{BA}\Delta X_C + X_{AB}\Delta Z_C + Z_{AB}\Delta X_D + X_{BA}\Delta Z_D \end{aligned} \quad (4)$$

¹We note that crease edges can be further divided into horizontal crease edges, which are expected to be more accurate than non-horizontal ones.

The second constraint, perpendicularity between lines, is achieved by constraining their scalar product to zero, and doing so leading to Equation 5:

$$\begin{aligned} ((X_B + \Delta X_B) - (X_A + \Delta X_A)) \cdot ((X_D + \Delta X_D) - (X_C + \Delta X_C)) \\ + ((Y_B + \Delta Y_B) - (Y_A + \Delta Y_A)) \cdot ((Y_D + \Delta Y_D) - (Y_C + \Delta Y_C)) \\ + ((Z_B + \Delta Z_B) - (Z_A + \Delta Z_A)) \cdot ((Z_D + \Delta Z_D) - (Z_C + \Delta Z_C)) = 0 \end{aligned} \quad (5)$$

This form can then be simplified in a similar fashion as for the parallelism constraint.

One merit of this adjustment form is that in the formation process, vertices that appear in close proximity to one another (defined by the point spacing) are merged unless a topological rule is violated. Therefore, this model also implicitly constrains lines of intersecting planes to meet in a common vertex (e.g., the apex of a tetrahedron shape).

Reconstruction Using Free Form Surfaces

When planar surface-based models are applied to curved surfaces, the reconstruction is likely to provide fractured (made of small/narrow) segments or a sporadic set of patches. We present in this section a model for their detection and reconstruction, beginning from a decision phase that analyzes whether surface patches originated from a curved face and then describe the geometric modeling of the face.

Segment Analysis and Detection of Curved Surfaces

The segmentation phase results in a set of planar patches, some relate to actual planar faces while others are parts of curved elements. The segment analysis process should therefore examine the utility in joining segments and decide which originate from a curved surface and which are planar by nature. A metric that facilitates this test can be based on grouping neighboring segments by fitting a high-degree parametric surface (e.g., a cubic surface), and given the two models (two individual planes or one high-degree surface) tell which model is preferable. In information theory, the best model to be chosen is the one that could compress the data to minimum memory volume. To choose the best model to represent the data one should consider both the goodness of fit and the complexity of the model. The measure we apply here is the Akaike Information Criterion (AIC) (Akaike, 1974; Boyer *et al.*, 1974) that takes both model complexity and modeling accuracy into consideration and has the advantage of being simple to apply. The AIC values, under normal distribution, are computed for each model using:

$$AIC = 2k + n \ln \frac{\sigma}{n} \quad (6)$$

with k , the number of parameters in the model, n , the number of points, and σ , the sum of the square errors (errors are the offsets of each point from the surface).

The evaluation is performed in a pair-wise manner, on neighboring segments, where for the AIC value is tested for the two individual planar segments against the merit of using one polynomial surface. Since the pair-wise evaluation does not aim reconstructing the actual shape of the complete curved surface (this is treated later on), the evaluation can be performed using a low-order polynomial. Experimenting with polynomial surfaces of degrees 2÷5 (number of parameters ranging between 6÷21) has shown that *locally*, bi-quadratic surfaces (six parameters) are sufficient to decide if the two surfaces under evaluation are in fact part of a curved surface. The low-degree polynomial has the advantage of limited flexibility in fitting surfaces (to avoid overfitting) while still fitting better to a curved surface than

two planar segments. We note that if concatenation would have taken effect, higher-order surfaces would be needed, and the evaluation procedure would have been far more complex (involving testing not only if the surfaces are curved or not, but also finding what degree accommodates their link).

The result of the evaluation procedure is a connectivity graph that links all the planar surface patches that constitute the curved surface elements.

Global B-Spline Surface Approximation

To join curved segments into a single roof face (or a whole roof), the chosen model should not impose restrictions on its shape. In this regard, Non-Uniform Rational B-Spline (NURBS) surfaces offer a mathematical representation that can accommodate and accurately describe surfaces of general shapes, ranging from simple 2D curves to complex free-form surfaces or solids. NURBS surfaces are ideal choice for curved or free-form building modeling as they are flexible, can accurately fit to a surface, and be rendered efficiently. Additionally, the amount of information required for NURBS representation, is much smaller than the one required by common facet based approximation. Since curves and surfaces behave in similar ways and share terminology, we outline the mathematical foundation of NURBS curves and then extend it to surfaces.

NURBS Description

A NURBS curve is defined by four properties: basis functions, degree, control points, and knots. The control points consist of at least “degree + 1” set of points and their placement dictates the shape of the curve. The control points have an associated weight that, with a few exceptions, is a positive number. Curves whose control points have similar weight (usually 1) are called non-rational, and otherwise rational. In practice, most NURBS curves are non-rational, while a few, like circles and ellipses as notable examples, are always rational. B-spline curves are described by:

$$c(u) = \sum_{i=0}^m P_{cp_i} B_{i,k}(u) = \begin{cases} X(u) = \sum_{i=0}^m X_{cp_i} \cdot B_{i,k}(u) \\ Y(u) = \sum_{i=0}^m Y_{cp_i} \cdot B_{i,k}(u) \\ Z(u) = \sum_{i=0}^m Z_{cp_i} \cdot B_{i,k}(u) \end{cases} \quad (7)$$

with $(X, Y, Z)_{cp_i}$, a control point, i , defining the curve, $B_{i,k}(u)$ the B-spline basis functions of degree k , for control point i . The basis functions define the B-spline continuity level where higher degree splines resulting in a higher continuity level of the piecewise curve. The degree, k , of the basis (blending) function will usually be one (linear), two (quadratic), three (cubic) or five (quintic), where most free-form curves are degree three or five (Cohen *et al.*, 2001; Farin, 2002). It is possible to increase the degree of a NURBS curve and not change its shape. It is not possible to reduce the degree of the NURBS curve without changing its shape.

The basis functions are defined recursively as:

$$B_{i,0}(u) = \begin{cases} 1 & \text{if } u_i \leq u < u_{i+1} \\ 0 & \text{otherwise} \end{cases} \quad (8)$$

$$B_{i,k}(u) = \frac{u - u_i}{u_{i+k} - u_i} B_{i,k-1}(u) + \frac{u_{i+k+1} - u}{u_{i+k+1} - u_{i+1}} B_{i+1,k-1}(u).$$

B-spline surfaces are defined as the product of two sets of basis functions of degree k and q defined by means of two independent parameters u and v :

$$s(u, v) = \sum_i \sum_j P_{cp(i,j)} B_{(i,k_u),(j,q_v)}(u, v) \quad (9)$$

Describing

$$B_{(i,k_u),(j,q_v)}(u, v) = B_{i,k_u}(u) N_{j,q_v}(v), \quad (10)$$

the tensor product B-spline surface of degree k and q can then be defined as:

$$s(u, v) = \sum_{i=0}^m \sum_{j=0}^n P_{cp(i,j)} B_{i,k_u}(u) N_{j,q_v}(v). \quad (11)$$

The $P_{cp(i,j)}$ coefficients present the control points and not points on the surface.

Global Surface Approximation

Generally, curves and surfaces can be described by means of interpolation or approximation. In case of interpolation, we require the curve to pass through the points P_1, P_2, \dots, P_n . In case of approximation, we require the curve to pass near the points P_1, P_2, \dots, P_n , with nearness defined in the least-squares sense, maximal difference, etc.

Consider a set of points $f_{i,j}$ $\{i = 1 \dots M, j = 1 \dots N\}$ for which a surface should be approximated using a tensor product. Given the basis functions, the problem can be formulated as finding a set of control points so that the square-error between the measured points and the approximated surface is minimal:

$$E = \sum_{i=0}^M \sum_{j=0}^N (f_{i,j} - s(u_i, v_j))^2 = \min. \quad (12)$$

The least-squares criterion can be achieved by differentiating E with respect to the control point $P_{I,J}$ (with I, J as fixed but an arbitrary pair of indices), which yields:

$$\begin{aligned} \frac{\partial E}{\partial P_{I,J}} &= 2 \sum_{i=0}^M \sum_{j=0}^N - (f_{i,j} - s(u_i, v_j)) \frac{\partial s(u_i, v_j)}{\partial P_{I,J}} \\ &= -2 \sum_{i=0}^M \sum_{j=0}^N (f_{i,j} - s(u_i, v_j)) B_I(u_i) N_J(v_j) \\ &= -2 \sum_{i=0}^M \sum_{j=0}^N f_{i,j} B_I(u_i) N_J(v_j) \\ &\quad + 2 \sum_{i=0}^M \sum_{j=0}^N s(u_i, v_j) B_I(u_i) N_J(v_j) \end{aligned} \quad (13)$$

By setting the partial derivatives to zero we have:

$$\begin{aligned} \sum_{i=0}^M \sum_{j=0}^N f_{i,j} B_I(u_i) N_J(v_j) &= \sum_{i=0}^M \sum_{j=0}^N s(u_i, v_j) B_I(u_i) N_J(v_j) \\ &= \sum_{i=0}^M \sum_{j=0}^N \left(\sum_{k=0}^m \sum_{q=0}^n P_{k,q} B_k(u_i) N_q(v_j) \right) B_I(u_i) N_J(v_j) \end{aligned} \quad (14)$$

$$= \sum_{k=0}^m \sum_{q=0}^n \left(\sum_{i=0}^M B_k(u_i) B_I(u_i) \right) P_{k,q} \left(\sum_{j=0}^N N_q(v_j) N_J(v_j) \right)$$

or

$$\sum_{i=0}^M \sum_{j=0}^N f_{i,j} B_I(u_i) N_J(v_j) = \sum_{k=0}^m \sum_{q=0}^n \left(\sum_{i=0}^M B_k(u_i) B_I(u_i) \right) P_{k,q} \left(\sum_{j=0}^N N_q(v_j) N_J(v_j) \right) \quad (15)$$

defining:

$$\begin{aligned} \mathbf{A}_{u[m \times M]} &:= a_{u,i=I,j=k} = \sum_{l=0}^M B_k(u_l) B_l(u_i) \\ \mathbf{A}_{v[N \times n]} &:= a_{v,i=J,j=q} = \sum_{l=0}^N N_q(v_l) N_j(v_i), \\ \mathbf{T}_{[M \times N]} &:= t_{I,J} = \sum_{i=0}^M \sum_{j=0}^N f_{i,j} B_I(u_i) N_J(v_j) \end{aligned} \quad (16)$$

the least-squares system can be written in a matrix notation as $\mathbf{T} = \mathbf{A}_u \mathbf{P} \mathbf{A}_v^T$ and solved by $\mathbf{P} = \mathbf{A}_u^{-1} \mathbf{T} (\mathbf{A}_v^T)^{-1}$. We note that solutions for uninvertible \mathbf{A}_v or \mathbf{A}_u cases exist, taking advantage of the of tensor-product surface approximation (see e.g., Cohen *et al.*, 2001).

For the surface approximation, the data has to be organized appropriately. This organization can be non-uniform but has to have the same number of measured points along the two principal directions. Since the raw laser data are not gridded, we define a set of evenly spaced profiles crossing the surface major direction. The points forming each profile are selected from a buffer created around it, and beginning and ending at the border edge. Therefore, the B-spline computation is performed on the original dataset.

Results and Discussion

Following the extension into free-form surfaces, the reconstruction model is general enough to support buildings of general shapes. We demonstrate this by focusing on two complex roof structures over which the standard reconstruction failed, and then discuss model selection matters. Finally, we present the application of the model on a general scene. For the demonstration we use data with different resolutions, ranging from fairly sparse (0.6 p/m²) to fairly dense (3 p/m²), and buildings with varying level of complexity.

Application of the Free Form Model

The application of the free-form model is demonstrated first on a hipped roof with one curved face (Figure 2). The point density of the laser data is ~ 1 p/m². For the segmentation,

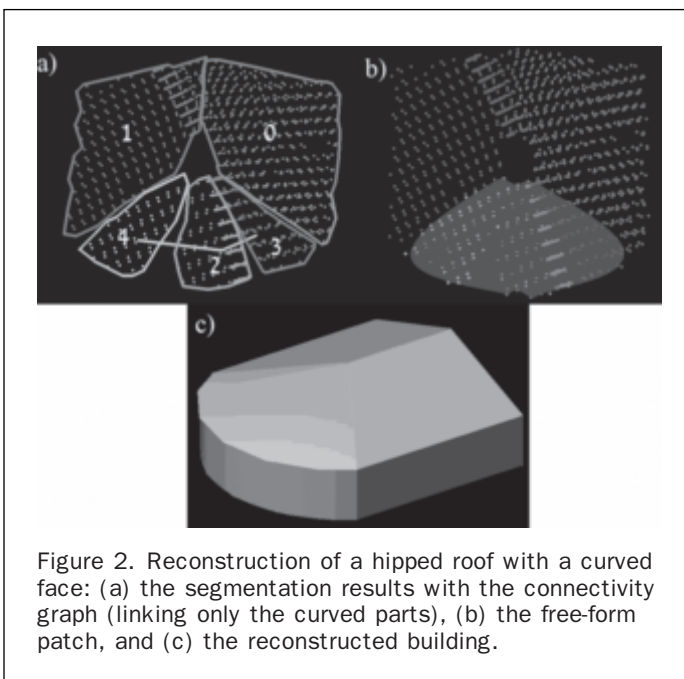


Figure 2. Reconstruction of a hipped roof with a curved face: (a) the segmentation results with the connectivity graph (linking only the curved parts), (b) the free-form patch, and (c) the reconstructed building.

TABLE 1. MODEL SELECTION USING THE AIC WITH THE SMALLEST AIC VALUES MARKED

Segment		AIC Values	
I	II	I + II	bi-quad. model
1	0	-6439	-1675
3		-4338	-2125
0	1	-6439	-1675
4		-3521	-1646
3	2	-2484	-2688
4		-1901	-2256
0	3	-4338	-2125
2		-2484	-2688
1	4	-3521	-1646
2		-1901	-2256

σ_{max} and σ_{min} were set to 15 cm and 5 cm, respectively, and segments with more than seven points were considered valid. These values are set by considering ranging accuracy, segment size, and redundancy with respect to the number of surface parameters. Figure 2a shows the results of the segmentation into planar faces. As the Figure shows, the segmentation identified the two wing-faces while the curved part was broken into three planar segments. In Table 1 the AIC values for each pair-wise evaluation are given, and when a curved pairing shows higher utility than keeping the two individual planes, the pair is marked as candidate for merging. The results show that the three surface segments that form the curved face have indeed a higher merit if joined together (again by evaluating neighboring pairs). The connectivity graph among the segments is shown in Figure 2a, and Figure 2b shows the free-form surface that was fitted to the three segments. The reconstructed model is shown in Figure 2c. The appearance of the free-form supported reconstruction is greatly improved than a fractured, plane-based one.

We turn into the reconstruction of a more complex roof that appears as the joining of two individual cone-like shapes. Figure 3a shows the raw points cloud. The point density of the laser data here is ~ 3 p/m². Figures 3b and 3c show the segmentation results for the free-form roof. For the segmentation σ_{max} was set to 15 cm, and the minimal number of points to 10 (relating to segment size and redundancy). The segmentation partitioned the roof into 32 plane segments that provide a fractured partitioning even though they cover the complete roof. The result of the surface-joining test is shown in Figure 3d in the form of a connectivity graph among segments. As can be seen, all segments were identified as belonging to a curved surface and all segments are connected (namely all segments compose one free-form surface). Merging the individual segments into one curved surface then follows. The result of the reconstruction by the NURBS surface-fitting is shown in Figure 3e. Compared to the fractured appearance that would have resulted if planar patches were to be used, this result is more visually pleasing, simple to render, and economic in terms of number of descriptive parameters.

Control Points for the NURBS Model

While the modeling part was demonstrated in the previous section, selection of the number of control points for the surface description is still left open. Generally, almost every free-form surface can be presented by NURBS with a degree varying between 3–5. However, the number of the control points can affect the resulting surface shape and accordingly

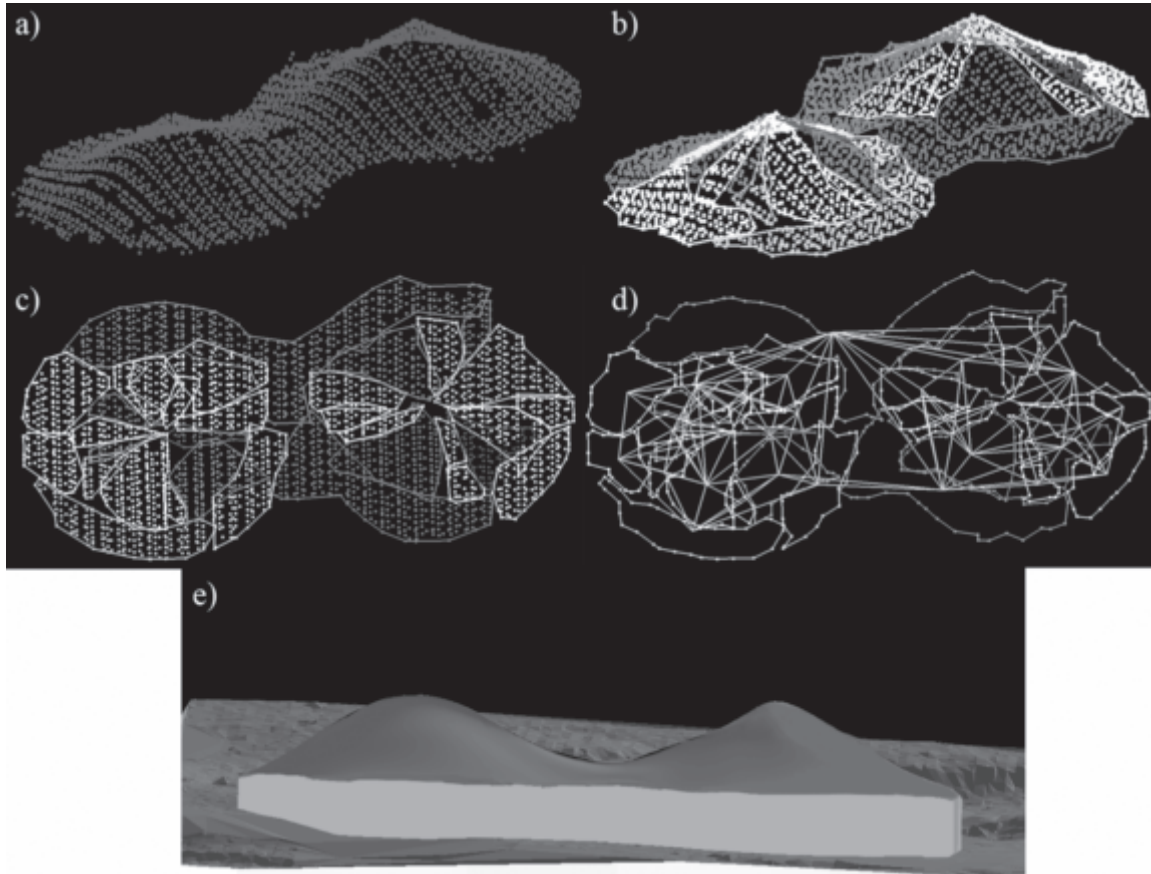


Figure 3. Reconstruction of a building with a free-form roof surface: (a) the point cloud of the roof, (b) the segmented point cloud from the same perspective, (c) the segmented data in down-looking view, (d) the connectivity graph between the segments, and (e) the reconstruction results

the fitting accuracy. The higher the number of the control points is, the smaller the residuals are between the surface points and the calculated NURBS. To select the optimal number of the control points for a given surface, we apply an iterative procedure that fits a NURBS surface and calculates the *std.* value of the fitting. In each iteration, the number of the points is increased and a new *std.* value is obtained. To determine the number of control points we apply two rules, the first evaluates the overall fitting accuracy and tests if the *std.* value has reached a prescribed value, the second evaluates the improvement gained by adding more control points in terms of the *std.* The termination criterion looks therefore at the *std.* value and the rate of improvement compared to the previous trial, namely:

$$std_i < \varepsilon \quad \& \quad \left| \frac{std_{i+1} - std_i}{std_{i+1}} \right| < t. \quad (17)$$

Figure 4 shows the decrease in the *std.* as a function of the number of control points for the building in Figure 3. The ε value was set to 20 cm, and was reached after seven iterations (increasing the number of control points by two between iterations) with an improvement rate between the last and penultimate iterations of 9 percent.

Demonstration on a Larger Scene

Finally, we demonstrate the application of the complete building reconstruction model on a large-scale urban scene

with a relatively low point-density of ~ 0.6 p/m². Figure 5a shows the shaded-relief view of the data. Overall, this neighborhood consists of 18 different buildings with diverse roof shapes that vary from simple (flat, saddleback, and cross-hipped roofs) to complex ones with a large number of asymmetric faces or free-form shaped roofs. The result of the filtering is presented in Figure 5b, which shows that the

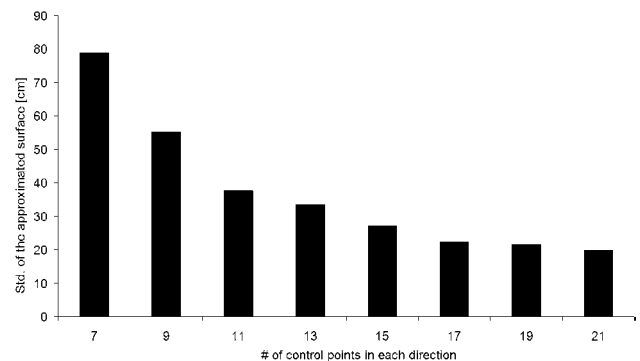


Figure 4. The decrease in the *std.* as a function of the number of control points for the building in Figure 3.

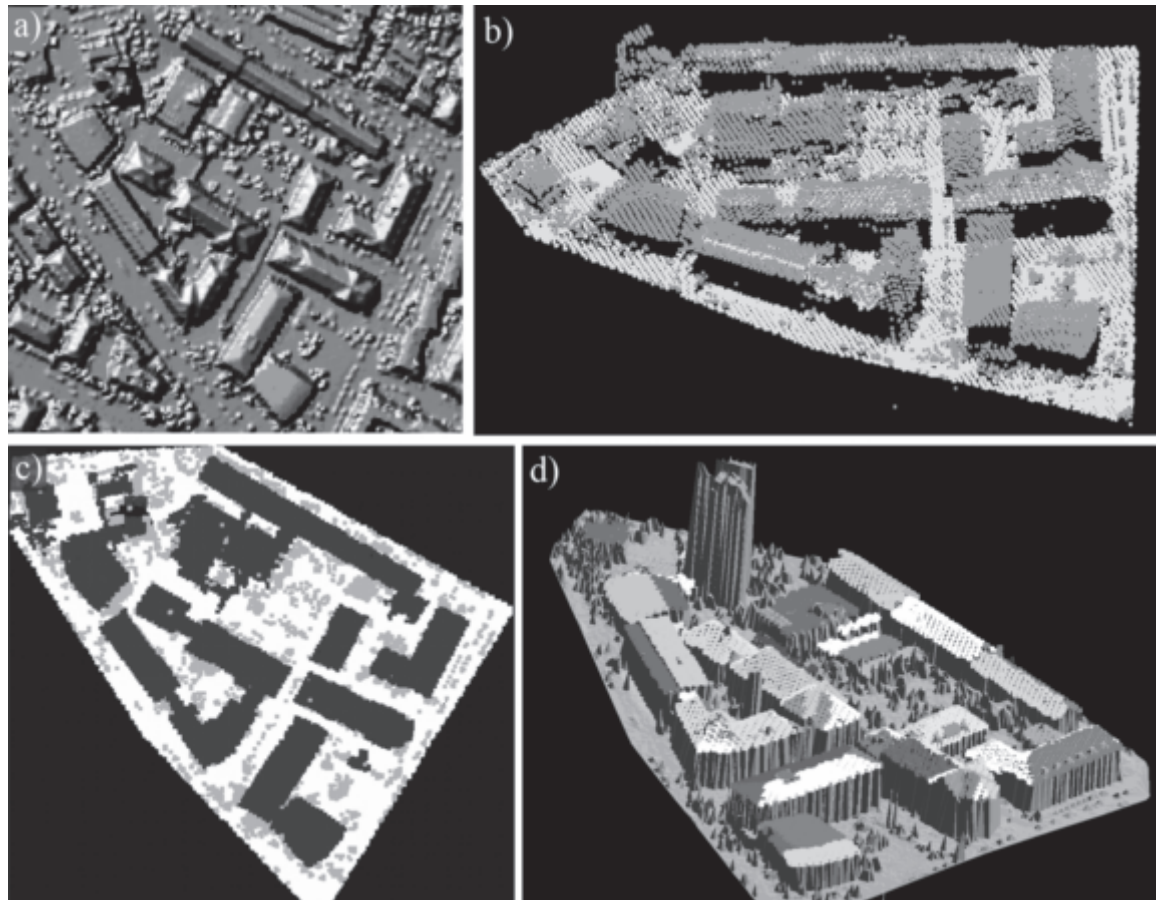


Figure 5. Processing lidar data of an urban scene with 0.6 p/m^2 point density: (a) a shaded-relief view of the data, (b) terrain and non-terrain classification, (c) results of the size and height based filtering, and (d) segmentation results.

buildings have been correctly classified as detached objects. Figure 5c that presents the result of the size and height based filtering shows that the non-building objects have been removed, thus saving the need to analyze them in the segmentation phase. Finally, Figure 5d shows the segmentation results.

We demonstrate in detail the reconstruction algorithm on three of the buildings whose shapes are complex. Figures 6a, 6c, and 6e show the point-sets of the three buildings following their segmentation. The segment boundaries are outlined and the topological relations between the faces are featured in the lines linking neighboring segments. All roof faces have been detected, though some dormers whose size was smaller than the minimal segment size (seven points) were not detected (applying a subsequent phase that locates cluster of points will add them in). The reconstruction results are shown in perspective view in Figures 6b, 6d, and 6f, respectively. Notice that the geometric adjustment of the building in Figure 6a did not link the two crease edges by a single node, even though they are in close proximity to one another and related by an orthogonality relation. This is attributed to the end-points adjustment and the node-linking criterion, which is distance aware and therefore avoids unnecessary joining. The following Figures (6c through 6f) demonstrate the result on others complex roofs. The result

in Figure 6c shows that the 13 dominant faces in the roof were identified. Notice that even though the apex of the dome is not part of any of the segments, it was correctly reconstructed following the adjustment and so is the outer boundary surrounding it.

Within the scene, two free-form roofs can be noticed (see encircled in Figure 7a and marked as I, and II). Figures 7b and 7e show the curved building points with the segmentation results. Again, as in the previous examples both roofs were broken into smaller segments. To demonstrate the free-form surface reconstruction we focus on the building marked as I. The segmentation results are shown in Figure 7e using an even larger value for the σ_{max} (set as high as 25 cm) that was applied to test how much the roof deviates from planarity. The application of the curve detection test on the segments is shown in connectivity graph (here reduced to a line) between the curved segments (see Figure 7e). To illustrate the utility of the reconstruction using free-form surfaces, we reconstruct the roof shape by using both the NURBS model and the plane partitioning. Figure 7d shows the results of the reconstruction using NURBS and for qualitative evaluation the TIN model of the original observations is drawn together with the reconstructed surface. For comparison, Figure 7f shows the result using the standard plane-based reconstruction. A comparison of the two results shows that while using NURBS, the residuals much more

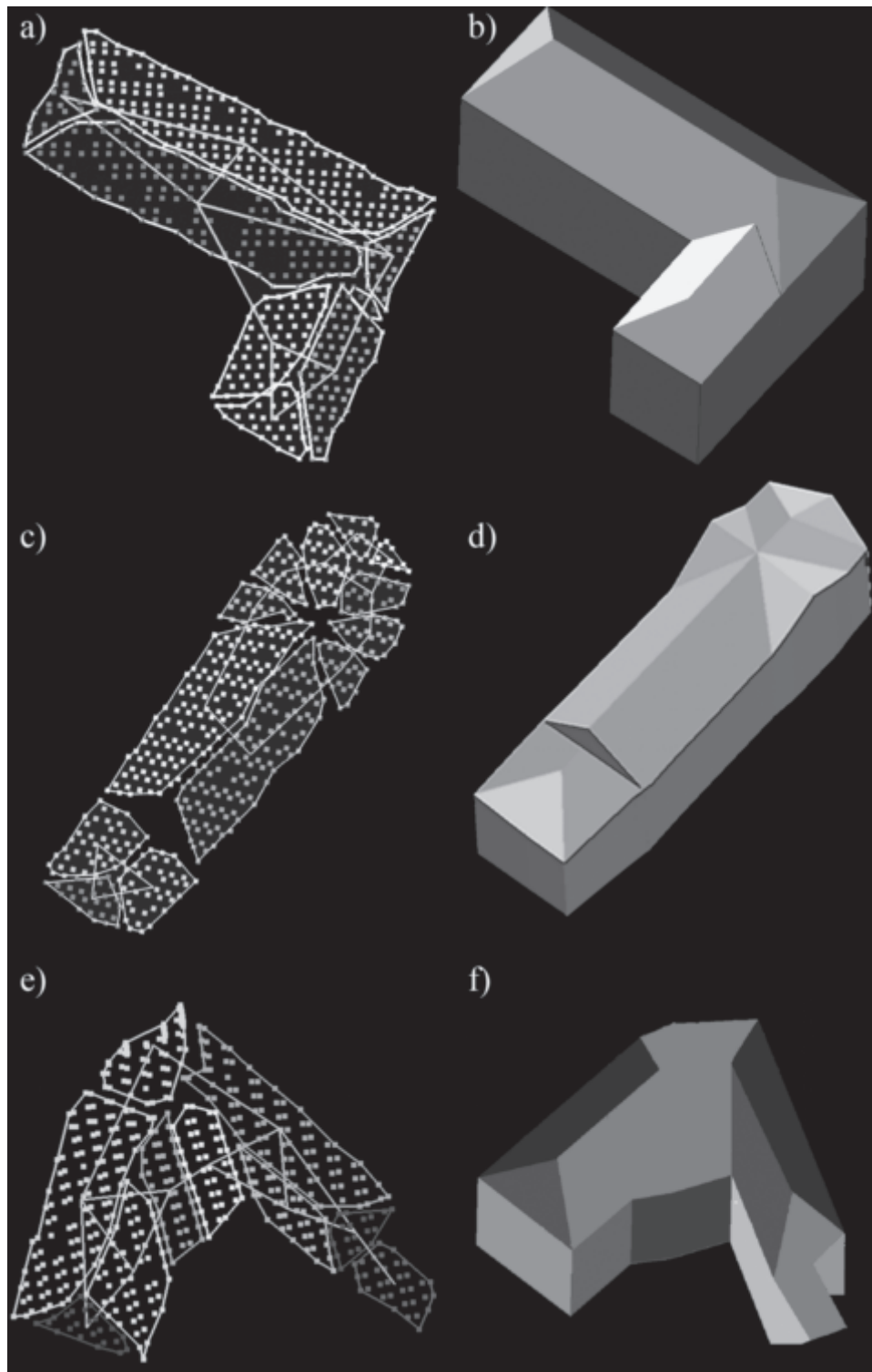
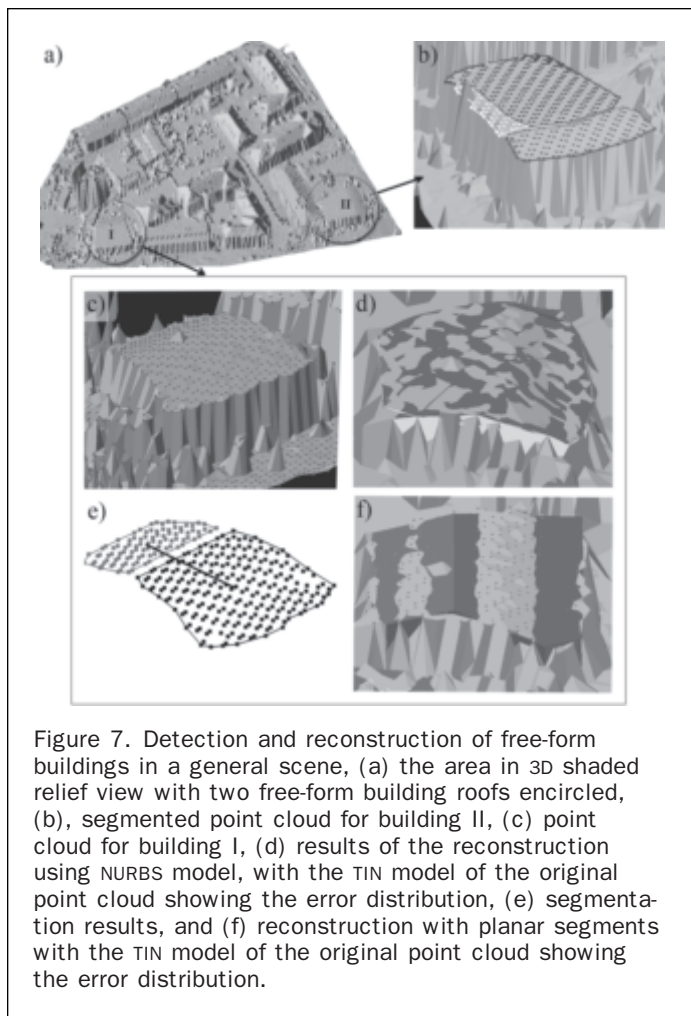


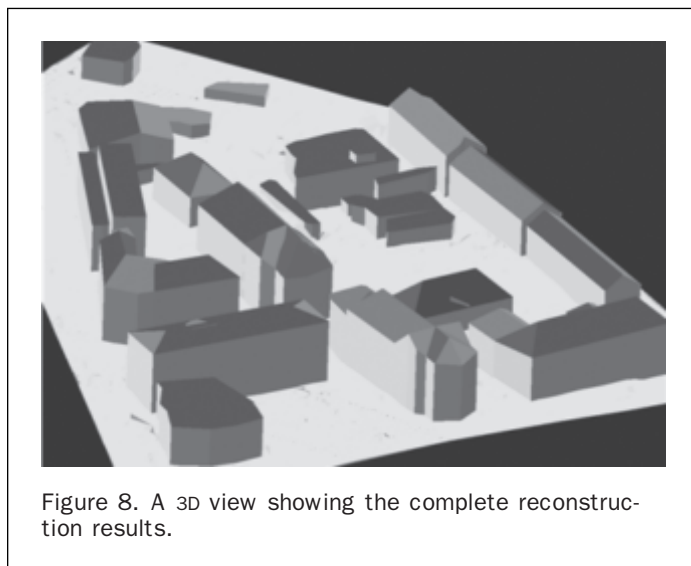
Figure 6. Reconstruction results of three complex buildings, (a, c, e) the segmented point cloud with segments boundary and the roof topology shown as links, (b, d, f) the reconstruction results.

randomly distributed than using the plane-based partitioning. With the plane-based reconstruction dominant clusters of positive and negative residuals are clearly shown, indicating the incapability in conveying the actual roof shape this way.

Finally, a 3D view of the results over the complete scene is shown in Figure 8. As can be seen, the buildings were correctly detected and reconstructed. We point to what may appear as a manmade object that was not detected already



in the first step; see Figure 5d. This undetected high-rise has a missing set of points that break it into two individual objects. The missing data at the middle of the roof makes it difficult for the algorithm to find dominant segments there. Potential approaches that can still manage detecting such



objects will add domain knowledge and consider maximal tree height as a parameter, and with lack of sufficient surface content assume a fixed height for that object.

Conclusions

This paper described an algorithm for reconstruction of building from laser scanning point clouds with no prior information. Differing from common algorithms, detection and reconstruction of curved surfaces is handled with the proposed model. The results show that the free-form roof surfaces representation offers a truer to reality model, and that such structures are not uncommon. They also show that the AIC measure is suitable to identify curved structures. The results also demonstrate the important role of the geometrical constraints on the reconstruction process. The experimental results have demonstrated that buildings can be correctly detected and reconstructed even with point density that is lower than what is commonly used.

References

- Akaike, H., 1974. A new look at the statistical model identification, *IEEE Transactions on Automatic Control*, 19:716–723.
- Abo Akel, N., S. Filin, and Y. Doytsher, 2007. Orthogonal polynomials supported by region growing segmentation for the extraction of terrain from lidar data, *Photogrammetric Engineering & Remote Sensing*, 73(11):1253–1266.
- Alharty, A., and J. Bethel, 2004. Detailed building reconstruction from airborne laser data using a moving surface method, *International Archives of Photogrammetry and Remote Sensing*, 35(B3):213–218.
- Boyer, K., M. Mirza, and G. Ganguly, 1994. The robust sequential estimator: A general approach and its application to surface organization in range data, *IEEE Transactions on PAMI*, 16(10):987–1001.
- Brenner, C., and N. Haala, 1998. Rapid acquisition of virtual reality city models from multiple data sources, *International Archives of Photogrammetry and Remote Sensing*, 32(5):323–330.
- Brenner, C., 2000. Towards fully automated generation of city boundary points will be clustered at the maximum if they are within a limited spacing and above a certain threshold models, *International Archives of Photogrammetry and Remote Sensing*, 33(3A):85–92.
- Cohen, E., R. Riesenfeld, and G. Elber, 2001. *Geometric Modeling with Splines: An Introduction*, A.K. Peters.
- Farin, G., 2002. *Curves and Surfaces for CAGD*, Fifth edition, Academic Press, Inc.
- Filin, S., and N. Pfeifer, 2006. Improved segmentation of airborne laser surfaces using adaptive distance based neighborhood, *ISPRS Journal of Photogrammetry and Remote Sensing*, 60(2):71–80.
- Kraus, K., and N. Pfeifer, 1998. Determination of terrain models in wooded areas with airborne laser scanner data, *ISPRS Journal of Photogrammetry and Remote Sensing*, 53:193–203.
- Haala, N., C. Brenner, and K.-H. Anders, 1998. 3D urban GIS from laser altimeter and 2D map data, *International Archives of Photogrammetry and Remote Sensing*, 32(3/1):339–346.
- Haala, N., S. Becker, and M. Kada, 2006. Cell decomposition for the generation of building models of multiple scales, *International Archives of the Photogrammetry, Remote Sensing and Spatial Information Sciences*, 36(3):19–24.
- Maas, H.-G., and G. Vosselman, 1999. Two algorithms for extracting building models from raw laser altimetry data, *ISPRS Journal of Photogrammetry and Remote Sensing*, 54(23):153–163.
- Mäntylä, M., 1988. *An Introduction to Solid Modeling*, Computer Science Press, Rockville, Maryland.
- Oda, K., T. Takano, T. Doihara, and R. Shibasaki, 2004. Automatic building extraction And 3-D city modeling from LiDAR data based on Hough Transform, *International Archives of Photogrammetry and Remote Sensing*, 35(B3):277–281.

- Rottensteiner, F., 2006, Consistent estimation of building parameters considering geometric regularities by soft constraints, *International Archives of the Photogrammetry, Remote Sensing and Spatial Information Sciences*, 36(3):13–18.
- Rottensteiner, F., J. Trinder, S. Clode, and K. Kubik, 2005. Automated delineation of roof planes from LIDAR data, *International Archives of the Photogrammetry, Remote Sensing and Spatial Information Sciences*, 36(3/W19):221–226.
- Schwalbe, E., 2004. 3D building model generation from airborne laserscanner data by straight-line detection in specific orthogonal projections, *International Archives of Photogrammetry and Remote Sensing*, 35(3):249–254.
- Seo, S., and T. Schenk, 2003, A study of integration methods of aerial imagery and LIDAR data for a high level of automation in 3D building reconstruction, *Proceedings of SPIE Aerosense 2003, Multisensor, Multisource Information Fusion: Architectures, Algorithms and Applications VII*, Orlando, Florida.
- Sithole, G., and G. Vosselman, 2004. Experimental comparison of filter algorithms for bare-earth extraction from airborne laser scanning point clouds, *ISPRS Journal of Photogrammetry and Remote Sensing*, 59(1–2):85–101.
- Voegtli, T., E. Steinle, and D. Tovari, 2005, Airborne laserscanning data for determination of suitable areas for photovoltaics, *International Archives of the Photogrammetry, Remote Sensing and Spatial Information Sciences*, 36(3/W19):215–220.
- Vosselman, G., 1999. Building reconstruction using planning faces in very high density height data, *Proceedings of the ISPRS Conference of Automatic Extraction of GIS Objects from Digital Imagery*, Munich, 08–10 September, pp. 87–92.
- Vosselman, G., and S. Dijkman, 2001. 3D building model reconstruction from point clouds and ground plans, *International Archives of Photogrammetry and Remote Sensing*, 34(3/W4):37–43.
- Wang, Z., 1998, Extracting building information from LIDAR data, *International Archives of Photogrammetry and Remote Sensing*, 32(3/1):279–284.
- Wang, Z., and T. Schenk, 2000. Building extraction and reconstruction from LiDAR data, *International Archives of Photogrammetry and Remote Sensing*, 33(B3):958–964.

(Received 29 May 2007; accepted 06 September 2007; revised 14 December 2007)